

ELECTROMAGNETIC SCATTERING FROM  
APPENDAGES ON A SMOOTH SURFACE

By

John L. Volakis\*, W. D. Burnside and L. Peters, Jr.  
The Ohio State University  
Electroscience Laboratory  
Columbus, Ohio 43212

ABSTRACT

A solution is obtained for the high frequency backscattered far field from appendages such as an inlet mounted on arbitrary smooth surfaces. The goal here is twofold; first, to demonstrate the effectiveness of the Uniform Geometrical Theory of Diffraction (UTD) in computing the scattered fields from such complex targets, and second, to develop iterative techniques to find multiply diffracted ray paths to be used in the application of UTD. These techniques are applicable to numerically as well as analytically defined surfaces.

---

\*Currently with the University of Michigan Radiation Laboratory, Department of Electrical Engineering and Computer Science, Ann Arbor, MI 48109.

## I. Introduction

Previous solutions based on the Uniform Geometrical Theory of Diffractions (UTD) [1] have mostly been applied to mathematically defined surfaces and structures. This paper presents generalized numerical ray-tracing routines which can be used for obtaining high frequency solutions to complex structures of arbitrary shape. The UTD along with the ray-tracing routines were used to determine the scattered fields from structures such as that shown in Fig. 1. The internal scattering from the hollow inlet is not included in this study. It is assumed that the reader is familiar with UTD which is discussed and developed sufficiently elsewhere [1,2].

In addition to the ordinary UTD, use is also made of the equivalent current concept [3,4,5] to account for the fields in the caustic regions. These exist when all the rays emanating from the perturbation, arrive at the observation point in phase. Because the caustic regions are usually associated with strong scattered fields, they tend to be dominant contributors.

The following solution will refer to the inlet structure and results will be given for the geometry shown in Fig. 2. However, the inlet can be of a more general shape, position and orientation. Further, the solution does not require an analytic description of the surface. Instead, given a surface, it is required that the surface normal ( $\hat{n}$ ), the principal surface radii ( $R_1$  and  $R_2$ ) and the corresponding unit directions ( $\hat{t}_1$  and  $\hat{t}_2$ ) be known. These can be supplied by any type of means from analytically or numerically defined surfaces. The backscattered fields with the same linear polarization are to be computed, but this is not a necessary case.

The region of interest is restricted to  $0^\circ < \theta < \theta_s$  and  $\phi < 90^\circ$ , where  $\theta_s$  corresponds to the shadow boundary of the inlet edge as shown in Fig. 3. In this region, the UTD solution includes the sum of the fields

produced by the ray paths indicated in Fig. 4. As noted above, the internal reflections in the inlet are ignored in this analysis. These have been discussed by various authors [6,7,8] for a circular inlet. Further, the results given later are for the xz plane of incidence.

## II. Outline of the UTD Solution

The UTD solution for the backscattered field has the following terms

$$\bar{E}^{\text{BSC}} = \bar{E}^{\text{GO}} + \bar{E}_1^{\text{D}} + 2\bar{E}_2^{\text{RD}} + \bar{E}_3^{\text{RDR}}, \quad (1)$$

where

$\bar{E}^{\text{GO}}$  = geometrical optics (GO) field

$\bar{E}_1^{\text{D}}$  = edge diffracted field from  $P_e^0$

$\bar{E}_2^{\text{RD}}$  = reflected-diffracted field through  $P_e^0$

$\bar{E}_3^{\text{RDR}}$  = reflected-diffracted-reflected field through  $P_e^0$ , and

$P_e^0$  is the stationary point on the inlet edge.

Note also that the factor of two multiplying  $\bar{E}_2^{\text{RD}}$  stands for the inclusion of the diffracted-reflected field ( $\bar{E}_2^{\text{DR}}$ ), since for plane wave incidence and for field calculations,

$$\bar{E}_2^{\text{DR}} = \bar{E}_2^{\text{RD}}. \quad (2)$$

The GO field is given by Eq. 8 of [1] for which the surface normal  $\hat{n} = -\hat{I}$ , where  $\hat{I}$  denotes the direction of incidence, and the edge diffracted field is given by Eq. (11) of [1] with the diffraction coefficients in Eq. (52) of the same reference. The reflected-diffracted field is computed in a similar manner to  $\bar{E}_1^{\text{D}}$ , except that the incident field to the edge will now be that reflected by the surface at  $S_r^0$ . Finally,  $\bar{E}_3^{\text{RDR}}$  is the field reflected from  $S_r^0$  when the incident field at this point is that obtained after reflection and then

diffraction. Note that in the case of  $\bar{E}_2^{RD}$  and  $\bar{E}_3^{RDR}$ , the generalized reflection coefficients (see Eq. (29), of [2]) have to be used near the shadow boundary. Not only is it necessary to evaluate the fields incident at the edge, but it is also necessary to evaluate the caustics associated with this reflection. These are needed to compute the appropriate distance parameter,  $L$ , and the caustic distance,  $\rho$ , which are used to obtain the edge diffracted fields. For a detailed derivation of the above field components the reader is referred to [9].

The calculated results for the radar cross section  $\sigma_{\phi\phi}$  and  $\sigma_{\theta\theta}$  in the  $xz$  plane of incidence are shown in Fig. 5. The term  $\bar{E}$  becomes indeterminate at  $\theta = 90^\circ$  for  $\sigma_{\phi\phi}$  and  $\bar{E}^{RD}$  at  $\theta \approx 67^\circ$  (in the pattern the infinity at  $\theta = 90^\circ$  is not apparent for  $\sigma_{\theta\theta}$  because the hard diffraction coefficient vanishes at this point). At these pattern points the caustic distance associated with the appropriate diffracted rays from the edge goes to infinity, and one can predict the location of this infinity by examining the expressions for the caustic distances. The UTD is invalid in the nearby region and needs to be supplemented by the equivalent current concept, since there are now an infinity of rays contributing to the scattering direction ( $-\hat{I}$ ). In the case of  $\bar{E}_2^{RD}$ , the reflected rays from a convex surface first diverge and then converge after diffraction, due to the edge curvature, so that the cone of diffracted rays at each edge point,  $P_e$ , contains one ray in the backscatter direction. This is illustrated in Fig. 6.

The third order field,  $\bar{E}_3^{RDR}$ , may also include a caustic region depending on the geometry under consideration. In this case, one of the principal radii of the reflected wavefront at  $S_r^0$  from the edge toward the backscatter direction may become infinite.

In order to obtain the scattered fields in the caustic regions, the equivalent current (EC) method was applied. This is a line integral approach and can also incorporate the field scattered by the discontinuities formed at the junctions of the edge with the surface (See Fig. 1). These will be referred as junction-corner fields and can represent a dominant contribution for the  $E_\theta$  polarization.

### III. Use of the EC Method

This approach is essentially that formulated by Ryan and Peters [4] and involves the placement of a set of electric and magnetic equivalent currents,  $I^e$  and  $I^m$  on the edge.

The equivalent currents used throughout the paper are generally defined by

$$\begin{Bmatrix} I^e \\ I^m \end{Bmatrix} = - \begin{Bmatrix} \frac{\hat{e} \cdot \bar{E}^*(0_e)}{Z_0} \\ (\hat{e} \times \hat{s}^*) \cdot \bar{E}^*(0_e) \end{Bmatrix} D_{\frac{S}{h}} \frac{2\sqrt{\lambda}}{\sin \beta_0^i} e^{-j\pi/4}$$

where  $\hat{e}$  is the unit vector tangent to the edge at each point  $P_e$ ,

$Z_0$  is the impedance of free space,

$0_e$  is the phase reference point as shown in Figure 2,

$D_{\frac{S}{h}}$  is the soft and hard diffraction coefficient in [1],

$$\cos \beta_0^i = \hat{s}^* \cdot \hat{e},$$

and  $\hat{s}^*$  with  $\bar{E}^*(0_e)$  denote the direction of the incident rays along the edge

and the associated incident field at the edge, respectively. The form of

these parameters depends on the ray mechanism (see Fig. 3) under evaluation.

For the singly diffracted field ( $\bar{E}^D$ ),  $\hat{s}^* = \hat{I}$ , the direction of the incident

rays from the far field source. Consequently,  $\bar{E}^*(0_e) = \hat{e}^I E^I(0_e)$ , where  $E^I$

is the field produced by these rays. In the case of the reflected-diffracted

field ( $\bar{E}^{RD}$ ) the field incident to the edge is that reflected by the surface as indicated in Fig. 4(b). Therefore,  $\hat{s}^* = \hat{s}^R$ , the direction of the reflected rays toward the edge and  $\bar{E}^*(0_e) = \bar{E}^R(0_e)$ , the associated reflected field. Formally, the equivalent currents for the reflected-diffracted-reflected field are those of the reflected-diffracted case but the diffraction coefficient  $D_s$  must be recomputed for each field component and in general at each edge point,  $P_e$ , since it is a function of the angle of incidence and diffraction, as well as the localized edge geometry.

The scattered fields are now found from

$$\begin{Bmatrix} \bar{E}^e \\ \bar{H}^m \end{Bmatrix} = - \int_{\text{edge}} I_{\text{edge}}^m \hat{e} \cdot \bar{K}^m d\mathbf{l}, \quad (4)$$

and the total field from the edge is given by

$$\bar{E} = \bar{E}^e + \bar{E}^m = \bar{E}^e + Z_0 (\bar{H}^m \times \hat{s}) \quad (5)$$

where  $\hat{s}$  is the direction of scattering. The spacial spreading factor may be explicitly represented if the kernel  $\bar{K}^m$  is written as

$$\bar{K}^m = \bar{g}^m \frac{e^{-jks}}{s} \quad (6)$$

The dyadic factor,  $\bar{g}^m$ , will now be dependent on the case being considered.

For the singly diffracted field,

$$\bar{g}^m = \begin{Bmatrix} Z_0 \hat{e} \hat{e} \\ -\hat{e}(\hat{s} \times \hat{e}) \end{Bmatrix} \frac{jk}{4\pi} e^{-j2k(\bar{P}_e - \bar{O}_e) \cdot \hat{I}} \quad (7)$$

where the variables  $\bar{P}_e$  and  $\bar{O}_e$  denote the vectors from the origin to the points  $P_e$  and  $O_e$ . In the case of the reflected-diffracted field,  $\bar{g}^m$  is again given by Eq. (7) since the direction of diffraction remains the same. However, for the reflected-diffracted-reflected field  $\bar{g}^m$  must be formulated

to account for the retracing of the ray back to the receiver. This is done by assuming an infinitesimal dipole source at each point of the edge as shown in Fig. 7. The dyadic factor for this case becomes

$$\overline{\overline{g}}^{e,m} = - \left\{ \begin{array}{l} Z_0 \hat{e}_\theta \\ \hat{e} (\hat{s} \times \hat{\phi}_e) \end{array} \right\} \cdot \overline{\overline{R}} \frac{1+jks^r}{4\pi(s^r)^2} \sin\theta_e \sqrt{\frac{\rho_{13}^3 \rho_{23}^3}{\rho_{13}^3 \rho_{23}^3}} e^{-jks^r} e^{-jk(\overline{S}_r - \overline{O}_e) \cdot \hat{I}}, \quad (8)$$

where

$$\hat{e}_\theta = \hat{s}^r \times \hat{\phi}_e,$$

$$\hat{\phi}_e = \hat{e} \times \hat{s}_p^r,$$

$$\theta_e = \cos^{-1}(-\hat{e} \cdot \hat{s}^r),$$

$\overline{\overline{R}}$  is the dyadic reflection coefficient as given in Eq. (29) of [2].

$s^r$  is the distance from the reflection point  $S_r$  to the diffraction point,  $P_e$ .

$\rho_{13,23}^3$  are the principal radii of the wavefront reflected off  $S_r$  after first being diffracted, and

$\hat{s}_p^r$  denotes the projection of the unit vector  $-\hat{s}^r$  onto the plane normal to  $\hat{e}$  (see Appendix A of [9]).

#### IV. Iterative Ray-Tracing

The formal solution presented thus far outlines briefly the electromagnetics involved in generating results by the EC method for the type of target under consideration. There remains the formidable computation of the various parameters which are functions of the target's geometry. The most difficult task here is to find the path of the ray that strikes the edge of the inlet after undergoing a reflection from the surface. Of course, this needs to be done at each edge point of the inlet for a given incident field direction. This is due to the integration required by the EC method as given in Eq. (4). The following outlines a numerical solution for computing these paths.

The direction of the reflected ray from the point of reflection at the curved surface is given by

$$(\bar{n} \times \hat{I})(\bar{s}^r \cdot \bar{n}) = - (\bar{n} \times \bar{s}^r)(\hat{I} \cdot \bar{n}) \quad (9)$$

and

$$\bar{s}^r = \bar{P}_e - \bar{S}_r, \quad (10)$$

where  $\bar{n}$  is a vector in the direction of the unit normal,  $\hat{n}$ . Evaluating  $\bar{S}_r$  is a difficult task for a general surface since an analytic expression for the surface normal may not be available or is too complex. An iterative solution that perturbs a known ray path as illustrated in Fig. 8 is attractive in this case. Such an approach has also been employed by Markefka [10] for finding multipaths between an analytic (cylindrical) surface and straight edges.

Assuming that the ray path, including the points  $S_r^0$  and  $P_e^0$ , is known (determination of such a path is discussed later), the surface may be approximated in the neighborhood of  $S_r^0$  by

$$z' = -1/2 \left[ \frac{x'^2}{R_1^0} + \frac{y'^2}{R_2^0} \right] \quad (11)$$

where

$$\text{and } \hat{x}' = \hat{t}_1^0, \quad (12a)$$

$$\hat{y}' = \hat{t}_2^0, \quad (12b)$$

$$\hat{z}' = \hat{n}^0 \quad (12c)$$

with  $\hat{t}_1^0$  and  $\hat{t}_2^0$  defining the principal surface directions at  $S_r^0$  and the corresponding principal surface radii of curvature being designated as  $R_1^0$  and  $R_2^0$ . Eq. (12) defines the primed coordinate system with origin at  $S_r^0$ .



Consequently, the surface normal at  $S_r^1$ , which is near  $S_r^0$ , can be approximated by

$$\bar{n}^1 \approx \frac{x'}{R_1^0} \hat{x}' + \frac{y'}{R_2^0} \hat{y}' + \hat{z}' \quad (13)$$

where

$$\bar{S}_r^1 = \hat{x}'x' + \hat{y}'y' + \hat{z}'z'. \quad (14)$$

Also,

$$\bar{s}_1^r = (P_{ex',-x'}^1)\hat{x}' + (P_{ey',-y'}^1)\hat{y}' + (P_{ez',-z'}^1)\hat{z}' \quad (15)$$

in which  $P_{ex',ey',ez'}^1$  are the components of the corresponding edge diffraction point,  $\bar{P}_e^1$ . To find the location of  $S_r^1$ , Eqs. (13) and (15) are substituted into Eq. (9) and it follows that

$$\begin{bmatrix} A_{11} & A_{12} \\ A_{21} & A_{22} \end{bmatrix} \begin{bmatrix} \frac{x'}{R_1^0} \\ \frac{y'}{R_2^0} \end{bmatrix} = \begin{bmatrix} C_{x'} \\ C_{y'} \end{bmatrix} \quad (16)$$

after neglecting higher order terms with respect to  $x'$  and  $y'$ . In this process the  $z$  components of Eq. (9) become negligible and thus one needs only to solve for  $x'$  and  $y'$  by Eq. (9) and then compute  $z'$  via Eq. (11).

The components of the above  $A$  matrix were found to be

$$A_{11} = -(I_{x',P_{ey'}^1} + I_{y',P_{ex'}^1}), \quad (17a)$$

$$A_{12} = -2I_{y',P_{ey'}^1} + 2I_{z',P_{ez'}^1} + I_{z',R_2^0}, \quad (17b)$$

$$A_{21} = -(-2I_{x',P_{ex'}^1} + 2I_{z',P_{ez'}^1} + I_{z',R_1^0}), \quad (17c)$$

$$A_{22} = -A_{11}, \quad (17d)$$

where  $I_{x',y',z'}$  are the components of the unit vector  $\hat{I}$  in the primed coordinate frame. In addition, for the C matrix one obtains

$$C_{x'} = I_{y'}P_{ez'}^1 + I_{z'}P_{ey'}^1, \quad (18a)$$

$$C_{y'} = -(I_{x'}P_{ez'}^1 + I_{z'}P_{ex'}^1). \quad (18b)$$

The above calculated  $S_r^1$ , is only a first order approximation of the true reflection point. Therefore, there is no assurance that  $S_r^1$  will be on the surface, albeit, it will be quite close to it. It is, of course, necessary to project the newly calculated reflection point on the surface to obtain  $S_{rp}^1$  which has this property. One is subsequently interested in the accuracy of  $S_{rp}^1$  as a representation of the true reflection point. To compute the associated error, the true normal ( $\bar{n}^1$ ) at  $S_{rp}^1$  and the reflected ray,

$$\bar{s}_1^r = \bar{p}_e^1 - \bar{S}_{rp}^1, \quad (19)$$

are substituted into Eq. (9) to obtain

$$(\bar{n} \times \hat{I})(\bar{s}_r^1 \cdot \bar{n}) = -(\bar{n} \times \bar{s}_r^1)(\hat{I} \cdot \bar{n}) + x'C_{ex'} + y'C_{ey'} + z'C_{ez'}, \quad (20)$$

where  $C_{ex'}$ ,  $C_{ey'}$ , and  $C_{ez'}$  denote the errors in the corresponding directions. Further, note that  $C_{ez'} \approx 0$  since as discussed earlier, the z-component of Eq. (9) does not contain any first order terms.

In order to evaluate the reflection point ( $S_r^2$ ) from which the reflected ray diffracts through the next integration point ( $P_e^2$ ), the above process is repeated with  $S_r^1$  and  $P_e^1$  as the initial points. However, one should be quite careful in continuing this iteration. The aforementioned errors will continue to increase due to the violation of our original assumption that the reflection law be satisfied at the reference (previous) point. But,

since these are available, Eq. (9) can be rewritten as

$$\begin{bmatrix} A_{11} & A_{12} \\ A_{21} & A_{22} \end{bmatrix} \begin{bmatrix} \frac{x'}{R_1^0} \\ \frac{y'}{R_2^0} \end{bmatrix} = \begin{bmatrix} C_{x'} + C_{ex'} \\ C_{y'} + C_{ey'} \end{bmatrix} \quad (21)$$

so that the errors are not propagated from one point to the next. The iterative process via Eq. (21) will be referred as the ray-tracing routine. Whenever  $C_{ex'}$ , and  $C_{ey'}$ , become unacceptably large (say greater than  $5 \times 10^{-3}$  for a 32-bit computer), it is an indication of a poor estimation of  $S_r$ . For a better result the ray-tracing routine may be repeated with the last computed reflection point as the reference, and with  $P_e$  and  $\hat{I}$  remaining constant.

Furthermore, although the above ray-tracing routine was derived for a variable  $P_e$ , it is also valid when  $\hat{I}$  is perturbed. This is essential for stepping from one pattern point calculation to the next provided  $\hat{I}$  changes a small amount (1-2 degrees). Therefore, only the knowledge of one reflected-diffracted ray path is needed in the whole pattern region. One such path is that for which the incident and diffracted rays from the inlet are normal to the surface at the projection of the edge diffraction point as demonstrated in Fig. 9. The path at the desired incidence is then found by perturbing the direction of this ray to the desired one.

#### V. Inclusion of Higher Order Mechanisms with the EC Method

The results by the EC method are shown in Fig. 10 for both polarizations of the incident wave for the same pattern cuts shown in Fig. 5 using the UTD solution. The  $\sigma_{\theta\theta}$  EC pattern indicates strong radar cross section (RCS) values near the nose-on region of the inlet. These are due to scattering by the junction-corners since the field polarization is parallel to the

inlet edge near the surface. Such behavior is not present in the UTD pattern of Fig. 5(b). The reader should also note that the UTD and EC patterns would be basically equal when away from the caustic regions, provided that junction-corner fields are included in the UTD solution.

For  $\theta > 90^\circ$ , part of inlet edge of Fig. 2 begins to become progressively shadowed and therefore the previous equivalent current expressions are not applicable for that portion of the edge. However, the EC solution could be extended to include the illumination of the edge in the shadow provided the observation point is in the far field as it occurs here.

This would require knowledge of the geodesic path from the point at which a creeping wave is launched on the surface to the point where it is shed, to in turn illuminate the shadowed portion of the edge. At the time this work was evolved, it was not feasible to find the geodesic for the general surface. Thus, a numerical extrapolation technique was used to approximately account for the scattering of the shadowed part. This method, although approximate, gave good agreement with the measured results when at least half of the edge was illuminated, provided that an appropriate predictor-interpolation algorithm was chosen. One such algorithm was a summation of shifted  $\frac{\sin x}{x}$  functions. Accordingly, the integrand of Eq. (4) in the shadow region is found by

$$\bar{E}_j^{e,m} \cdot \hat{e}^I = \sum_{i=0, N, 2N, \dots} \bar{E}_i^{e,m} \cdot \hat{e}^I \frac{\sin[(\pi/d\lambda^i) |\bar{p}_e^j - \bar{p}_e^i|]}{(\pi/d\lambda^i) |\bar{p}_e^j - \bar{p}_e^i|} \quad (22)$$

where  $\bar{p}_e^i$  is the  $i^{\text{th}}$  sampling point on the rim. The calculated integrand is given by  $\bar{E}_i^{e,m}$  at  $\lambda = \bar{p}_e^i$  and  $\bar{E}_j^{e,m}$  corresponds to the predicted component at  $\lambda = \bar{p}_e^j$ . Note also that

$$d\lambda^i = |\bar{p}_e^{i+1} - \bar{p}_e^i| \quad (23)$$

where  $N$  is an integer greater or equal to one and satisfies Nyquist's theorem. For  $N > 1$ , a smaller number of predicted field points are needed for the prediction of the following point and thus the accuracy of the algorithm is increased.

#### VI. Comparison Between Theory and Experiment

Measured data were taken at 9.01GHz using the model in Fig. 11. Absorber was positioned as illustrated to eliminate internal reflections and multiple diffraction at the back. However, first and second order diffraction from point  $P_e^{b0}$  was included in the analysis (see Appendix B of [9] for details).

The calculated and measured results for the model in Fig. 11 are given in Fig. 12. Excellent agreement is observed between theory and experiment for both polarizations of incidence considering the complexity of the model, the difficulty in the alignment and the approximations in the analysis.

#### V. Concluding Remarks

Although the results presented in this paper were restricted to a cylindrical inlet over an ogive, the EC method can be applied in the lit region of any type of edge over a smooth surface for which the surface normal, the principal radii and the corresponding directions can be computed. In addition, the EC method can be used for finding the fields caused by the aforementioned diffraction mechanisms (edge diffracted, reflected-diffracted, reflected-diffracted-reflected) at any desired pattern cut. However, one should be careful to note that additional dominant backscattering mechanisms will appear when in the broadside region, for example, of a plate mounted over a smooth surface. These include the

doubly reflected ray between the surface and the plate or scattering from the junction of the plate with the surface. The last is dominant when the plate is normal to the surface. These mechanisms will be discussed in more detail in future publication.

#### Acknowledgement

The authors wish to thank Professor Jack H. Richmond for his helpful discussions on the predictor-interpolator algorithm.

References

1. R. G. Kouyoumjian and P. H. Pathak, "A uniform geometrical theory of diffraction for an edge in a perfectly conducting surface," Proc. of the IEEE, Vol. 62, pp. 1448-1461, Nov. 1974.
2. P. H. Pathak, W. D. Burnside, and R. J. Marhefka, "A uniform GTD analysis of the diffraction of electromagnetic waves by a smooth convex surface," IEEE Trans. on Antennas and Propagat., Vol. AP-28, pp. 631-642, Sept. 1980.
3. R. F. Millar, "An approximate theory of the diffraction of an electromagnetic wave by an aperture in a plane screen," Proc. of the IEE, Vol. 103C, pp. 177-185, 1956.
4. C. E. Ryan and L. Peters, Jr., "Evaluation of edge-diffracted fields including equivalent currents for the caustic regions," IEEE Trans. on Antennas and Propagat., Vol. AP-17, pp. 292-299, May 1969; see also correction to this paper in Vol. AP-18, p. 275, March 1970.
5. E. F. Knott and T.B.A. Senior, "Equivalent currents for a ring discontinuity," IEEE Trans. on Antennas and Propagat., Vol. AP-21, pp. 693-695, Sept. 1973.
6. C. A. Chuang, C. S. Liang and S. W. Lee, "High frequency scattering from an open ended semi-infinite cylinder," IEEE Trans. Antennas and Propagat., Vol. AP-23, No. 6, pp. 770-776, Nov. 1975.
7. T. W. Johnson, "Electromagnetic scattering by open circular waveguides," Ph.D. Dissertation, The Ohio State University, Dept. of Electrical Engineering, 1980.
8. C. C. Huang, "Ray analysis of EM backscatter from jet intake configurations," Ph.D. Dissertation, The Ohio State University, Dept. of Electrical Engineering, 1982.

9. J. L. Volakis, "Electromagnetic scattering from inlets and plates mounted on arbitrary smooth surfaces," Ph.D. Dissertation, The Ohio State University, Dept. of Electrical Engineering, 1982.
10. R. J. Marhefta, "Analysis of aircraft wing-mounted antenna patterns," Ph.D. Dissertation, The Ohio State University, Dept. of Electrical Engineering, 1976.



## LIST OF FIGURES

1. Sketch of an arbitrary thin-edge inlet over a surface.
2. Geometry of a semi-infinite hollow cylinder over an ogive.
3. Illustration of the shadow boundary of an inlet structure.
4. Illustration of the dominant mechanisms associated with an edge over a surface (a) zeroth and first order mechanisms, (b) higher order mechanisms.
5. Calculated  $\sigma_{\phi\phi}$  and  $\sigma_{\theta\theta}$  RCS patterns from the structure in Figure 2 by the UTD with  $R_1=12.073"$ ,  $\alpha=46.34^\circ$ ,  $a=2.1"$ , and  $\lambda=1.311"$ . (a)  $\sigma_{\phi\phi}$ ,  $\phi=0$  pattern (b)  $\sigma_{\theta\theta}$ ,  $\phi=0$  pattern.
6. Illustration of the caustic associated with the reflected-diffracted field.
7. Radiation of the equivalent current in the backscatter direction when associated with the reflected-diffracted-reflected mechanism.
8. Illustration of the raytracing routine.
9. Raytracing of the reflection point when the incident ray is varied from  $\hat{I}^K$  to  $\hat{I}$ .
10. Calculated  $\sigma_{\phi\phi}$  and  $\sigma_{\theta\theta}$  RCS patterns from the structure in Figure 2 by the EC method;  $R_1=12.073"$ ,  $\alpha=46.34"$ ,  $a = 2.1"$ , and  $\lambda=1.311"$ . (a)  $\sigma_{\phi\phi}$ ,  $\phi=0$  pattern (b)  $\sigma_{\theta\theta}$ ,  $\phi=0$  pattern.
11. Geometry of the model of the structure in Figure 2 used for measurements.
12. Comparison of measured and calculated  $\sigma_{\phi\phi}$  and  $\sigma_{\theta\theta}$  RCS patterns from the model in Figure 1) with  $\lambda=1.311"$ . (a)  $\sigma_{\phi\phi}$ ,  $\phi=0$  pattern (b)  $\sigma_{\theta\theta}$ ,  $\phi=0$  pattern.

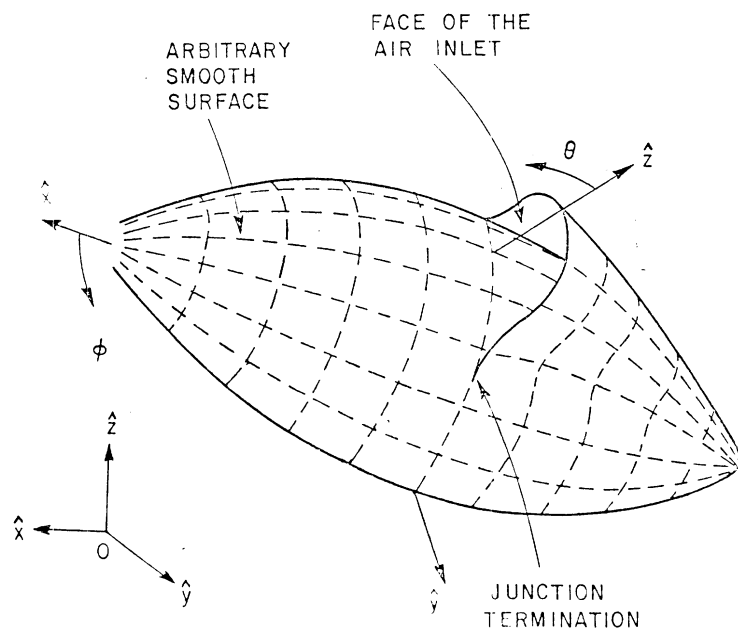


Figure 1. Sketch of an arbitrary thin-edge inlet over a surface.

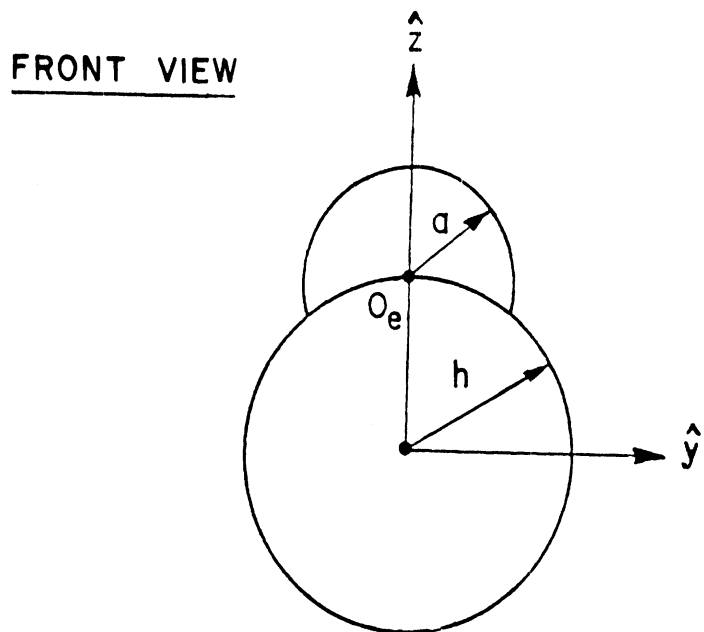
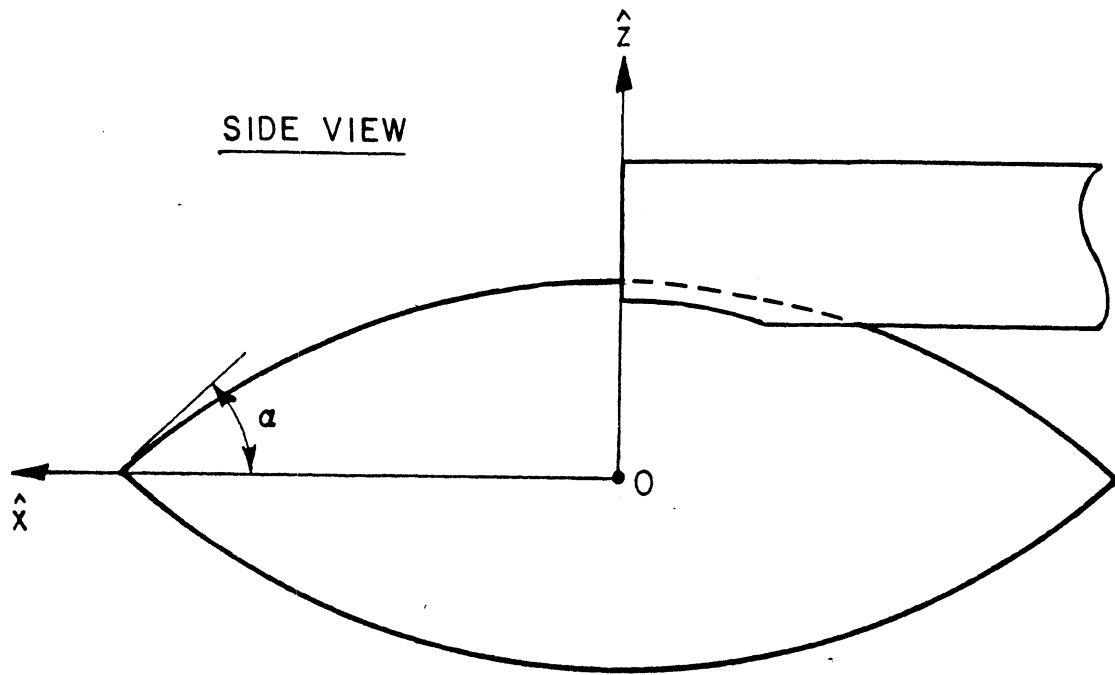


Figure 2. Geometry of a semi-infinite hollow cylinder over an ogive.

*Figure 2*

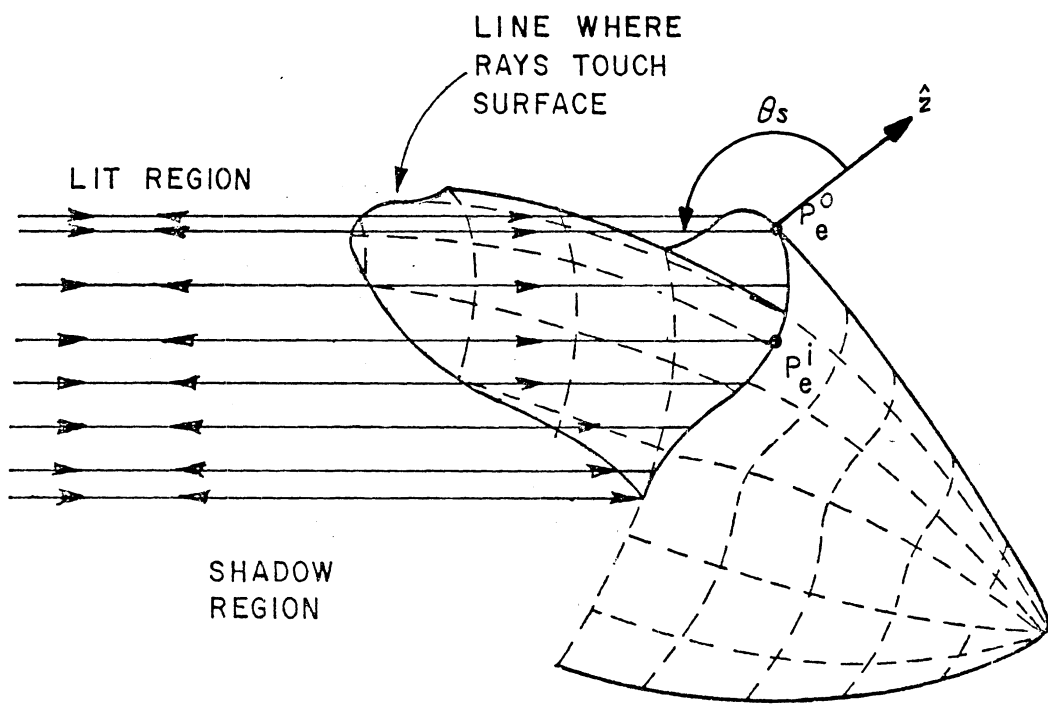


Figure 3. Illustration of the shadow boundary of an inlet structure.

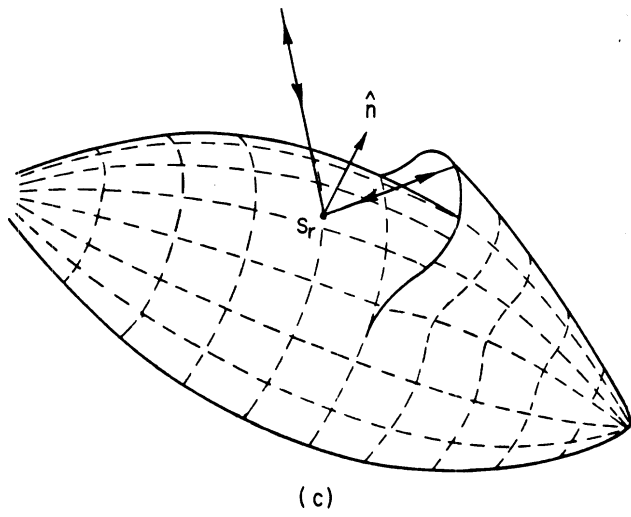
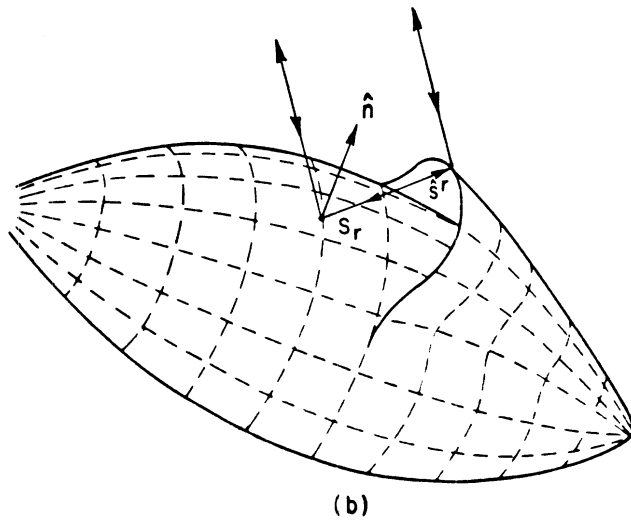
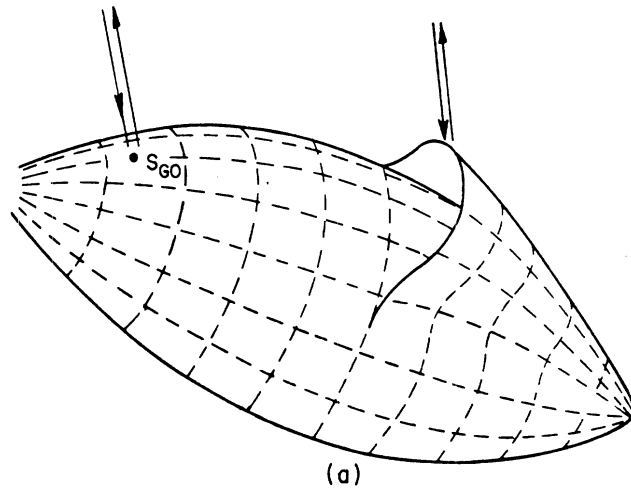


Figure 4

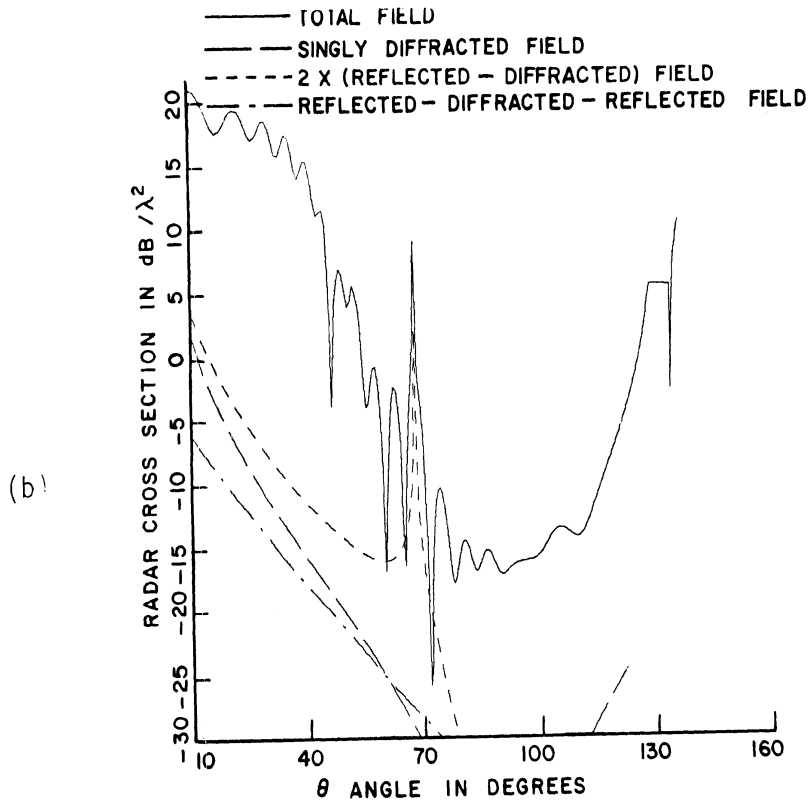
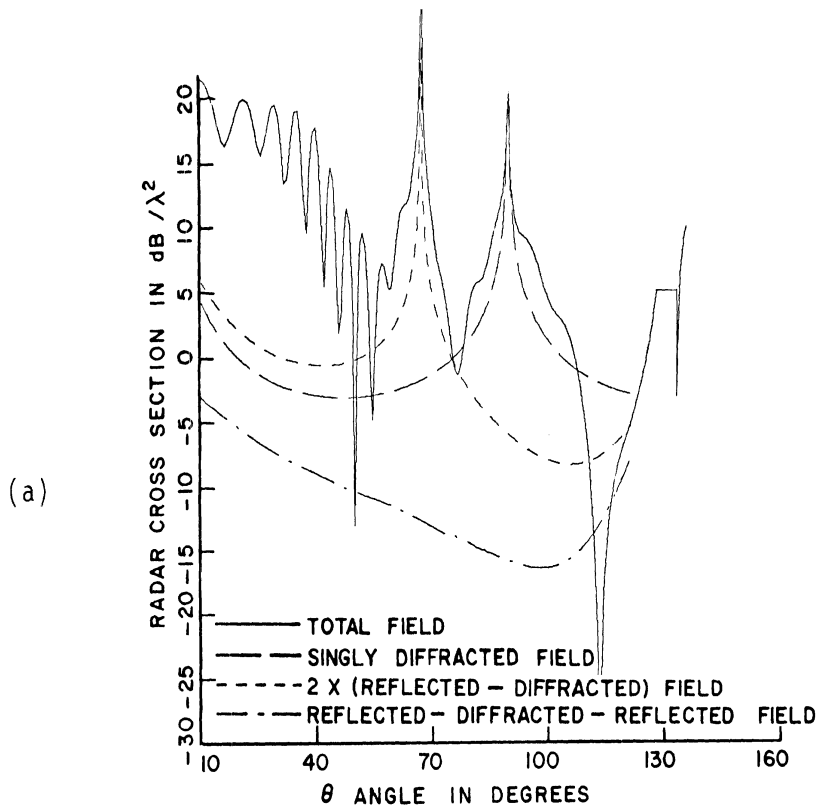


Figure 5. Calculated  $\sigma_{\phi\phi}$  and  $\sigma_{\theta\theta}$  RCS patterns from the structure in Figure 2 by the UTD with  $R_1=12.073''$ ,  $\alpha=46.34^\circ$ ,  $a=2.1''$ , and  $\lambda=1.311''$ .  
 (a)  $\sigma_{\phi\phi}$ ,  $\phi=0$  pattern (b)  $\sigma_{\theta\theta}$ ,  $\phi=0$  pattern.

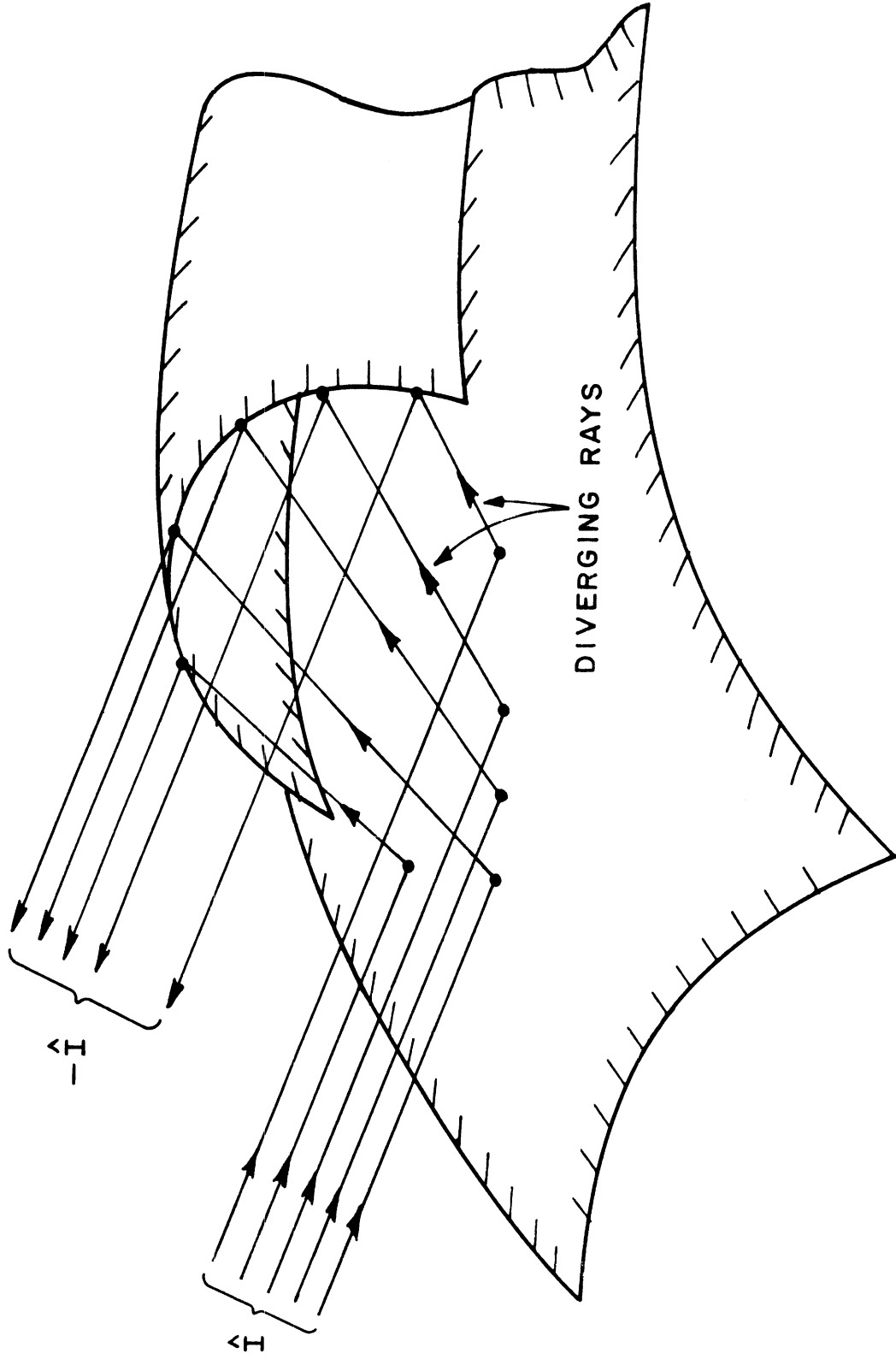


Figure 6. Illustration of the caustic associated with the reflected-diffracted field.

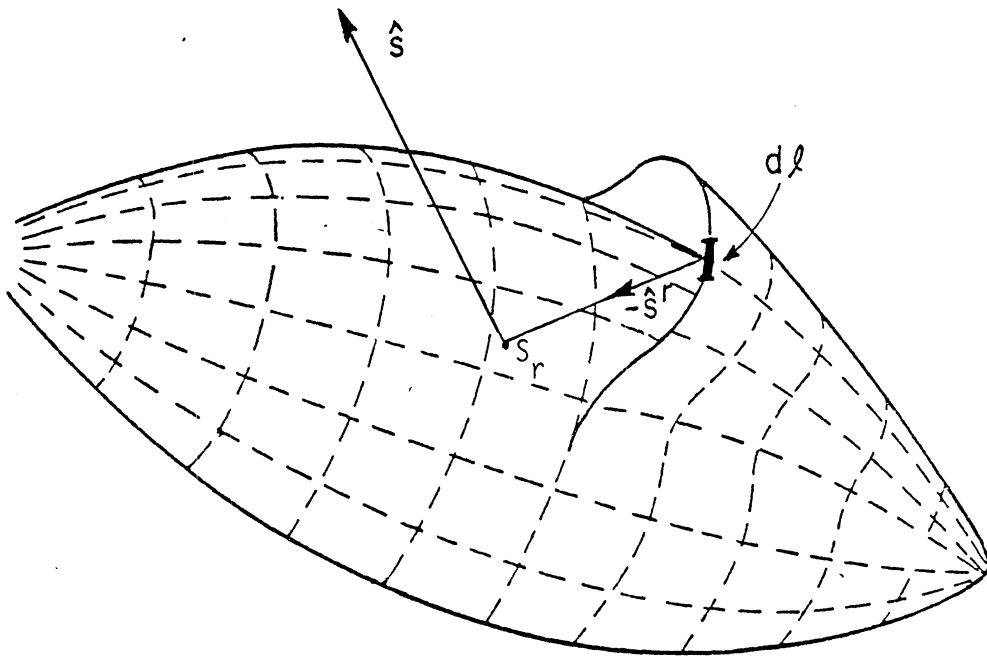


Figure 7. Radiation of the equivalent current in the backscatter direction when associated with the reflected-diffracted-reflected mechanism.



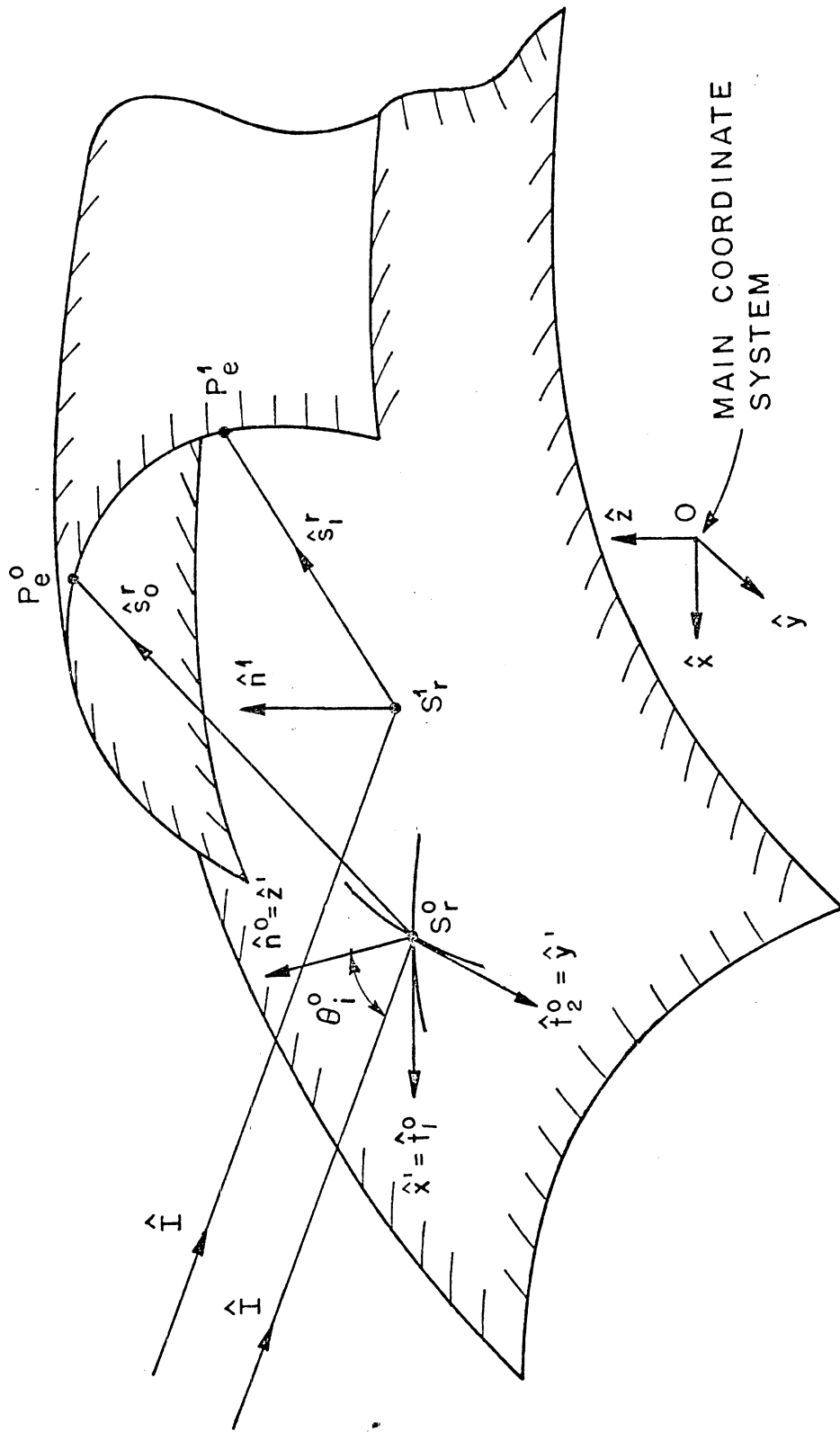


Figure 8. Illustration of the raytracing routine.

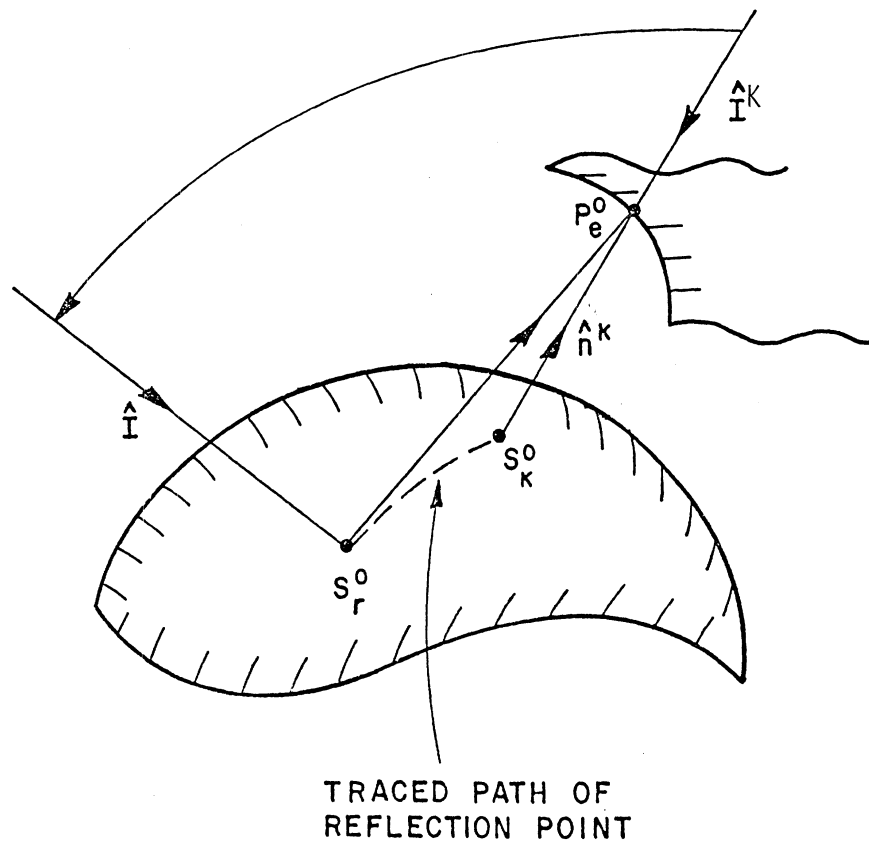


Figure 9. Raytracing of the reflection point when the incident ray is varied from  $\hat{I}^k$  to  $\hat{I}$ .

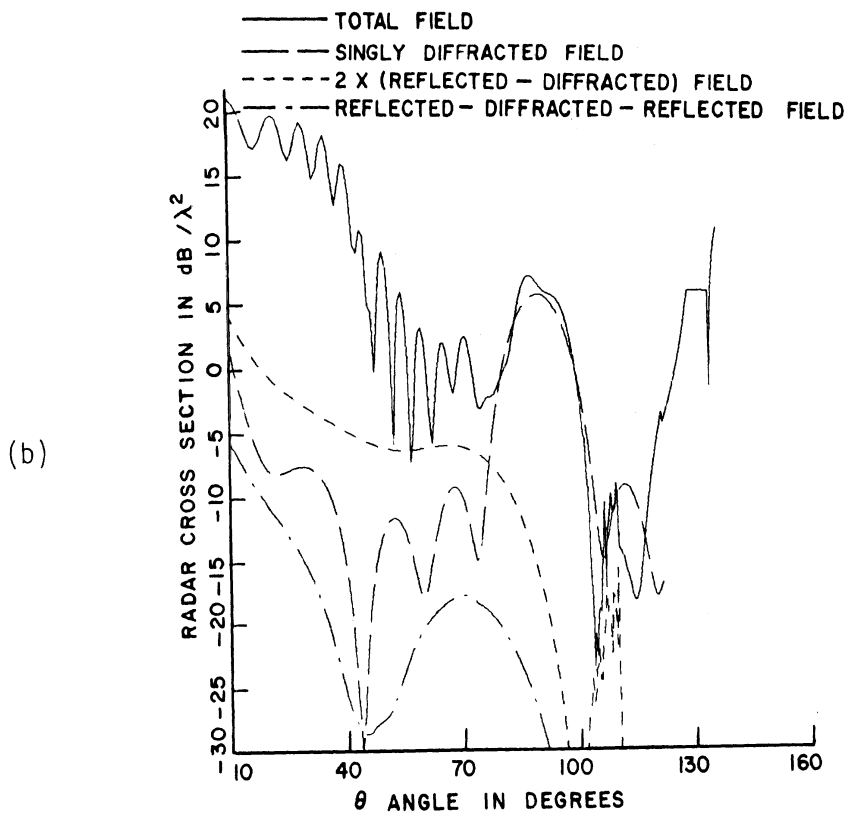
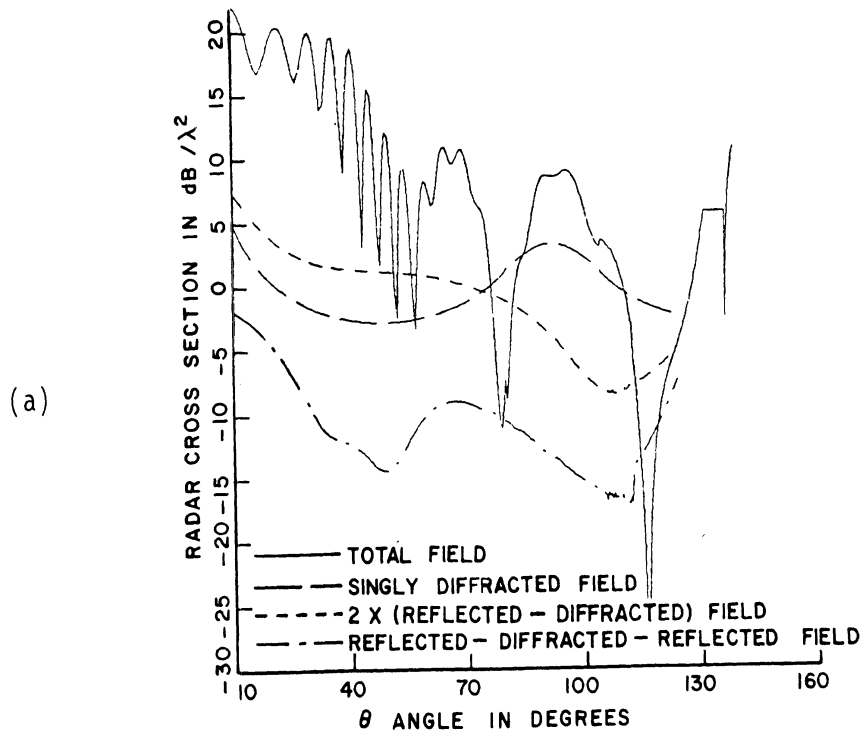


Figure 10. Calculated  $\sigma_{\phi\phi}$  and  $\sigma_{\theta\theta}$  RCS patterns from the structure in Figure 2 by the EC method;  $R_1=12.073''$ ,  $\alpha=46.34''$ ,  $a = 2.1''$ , and  $\lambda=1.311''$ . (a)  $\sigma_{\phi\phi}$ ,  $\phi=0$  pattern (b)  $\sigma_{\theta\theta}$ ,  $\phi=0$  pattern.

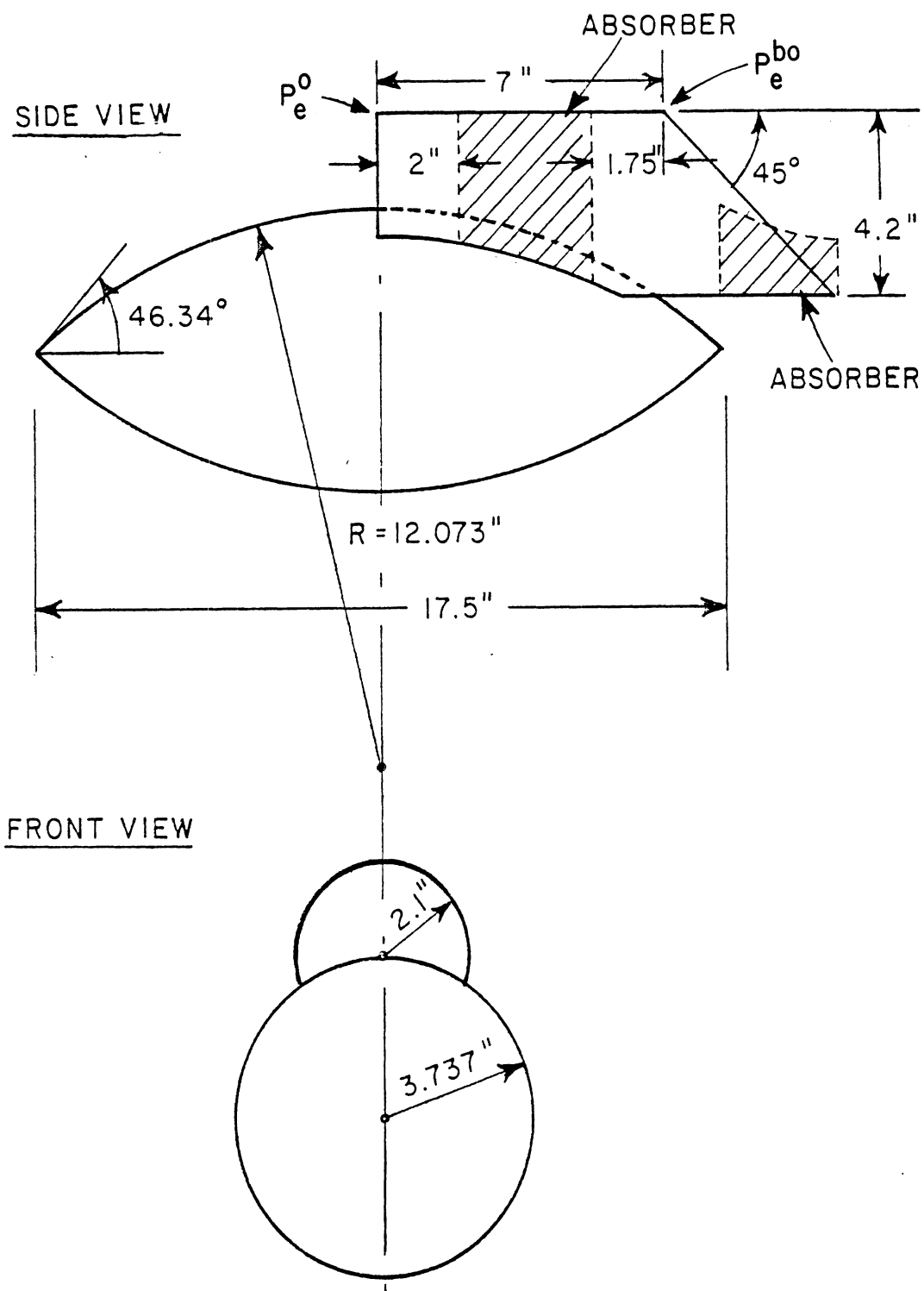


Figure 11. Geometry of the model of the structure in Figure 2 used for measurements.

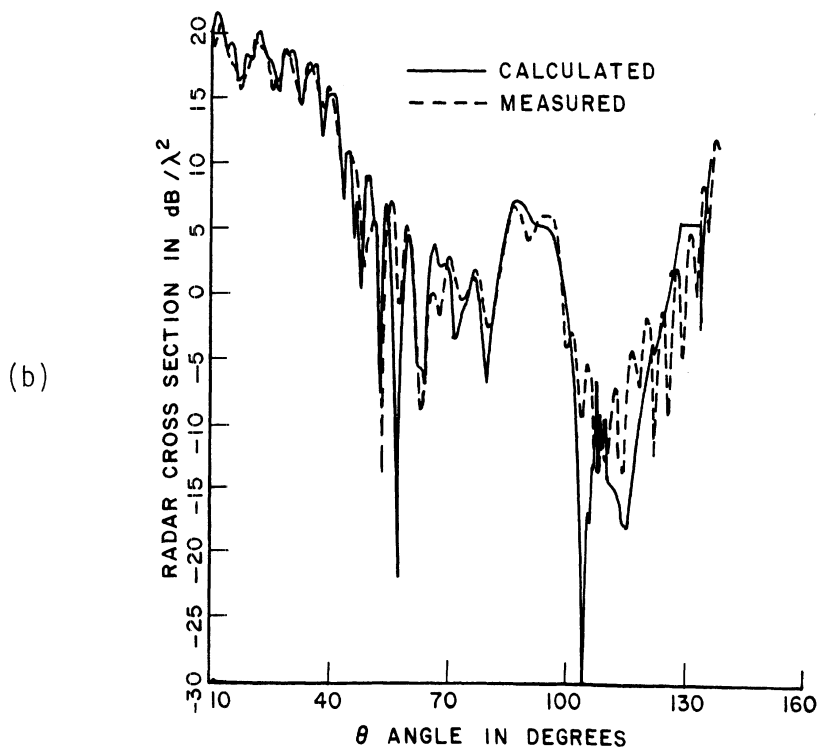
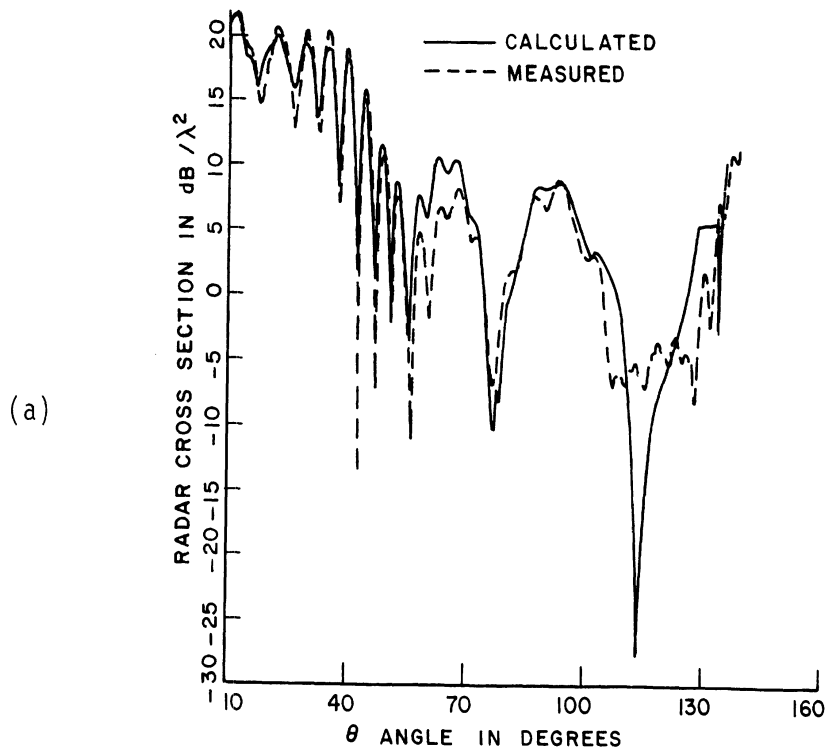


Figure 12. Comparison of measured and calculated  $\sigma_{\phi\phi}$  and  $\sigma_{\theta\theta}$  RCS patterns from the model in Figure 11 with  $\lambda=1.311''$ .

(a)  $\sigma_{\phi\phi}$ ,  $\phi=0$  pattern (b)  $\sigma_{\theta\theta}$ ,  $\phi=0$  pattern.